Flux expulsion in niobium superconducting radio-frequency cavities of different purity and essential contributions to the flux sensitivity

P. Dhakal,[1,*] G. Ciovati,[1,2] and A. Gurevich[2]

[1] *Thomas Jefferson National Accelerator Facility, Newport News, VA 23606, USA*
[2] *Center for Accelerator Science, Department of Physics, Old Dominion University, Norfolk, Virginia 23529, USA*

(Dated: May 29, 2019)

Magnetic flux trapped during the cooldown of superconducting radio-frequency cavities through the transition temperature due to incomplete Meissner state is known to be a significant source of radio-frequency losses. The sensitivity of flux trapping depends on the distribution and the type of defects and impurities which pin vortices, as well as the cooldown dynamics when the cavity transitions from a normal to superconducting state. Here we present the results of measurements of the flux trapping sensitivity on 1.3 GHz elliptical cavities made from large-grain niobium with different purity for different cooldown dynamics and surface treatments. The results show that lower purity material results in a higher fraction of trapped flux. We present an overview of published data on the mean free path and frequency dependence of the trapped flux sensitivity which shows a significant scatter which highlights the complexity of the pinning phenomenon on a bulk superconductor with a large curved surface. We discuss contributions of different physical mechanisms to rf losses resulting from oscillations of flexible vortex segments driven by weak rf fields. In particular, we address the dependence of the rf losses on the mean free path in the cases of sparse strong pinning defects and collective pinning by many weak defects for different orientations of the vortex with respect to the inner cavity surface. This analysis shows that the effect of the line tension of vortices is instrumental in the physics of flux trapping and rf losses, and theoretical models taking into account different pinning strength and geometry of flexible pinned vortex segments can provide a good qualitative description of the experimental data.

I. INTRODUCTION

The performance of superconducting radio-frequency (SRF) cavities is measured in terms of the dependence of the unloaded quality factor $Q_0 = G/R_s$ on the accelerating gradient, E_{acc}, where a geometric factor G depends on the cavity geometry, and $R_s(E_{acc})$ is an average surface resistance. At GHz frequencies the penetration depth of the rf field at the inner surface of the cavity is close to the static London penetration depth λ which is of the order of 40 nm in niobium. Recent advances in the processing of bulk niobium cavities have resulted in significant improvements of the quality factor and reducing the temperature-dependent surface resistance via diffusion of impurities over a few micrometers from the inner surface of the cavities [1, 2].

It has been shown both experimentally and theoretically that additional rf losses result from a residual magnetic flux trapped in the superconductor in the form of quantized magnetic vortices during the cavity cooldown through the superconducting transition temperature, T_c. Understanding the physics of this process is important to minimize the amount of trapped magnetic flux and thus maximize the cavity quality factor and reduce the cryogenic losses. For instance, it was found that the amount of trapped flux is affected by the cooling rate, as well as the magnitude and direction of the temperature gradient during the cavity transition to the superconducting state [3–8].

The typical material used for the fabrication of SRF cavities is bulk, $3-5$ mm thick, fine-grain (~ 50 μm average grain size) niobium with the normal state residual resistivity ratio (RRR) of ~ 300. Large-grain niobium, with grain size typically greater than ~ 1 cm, is an alternative material for the fabrication of SRF cavities [9]. One study showed that the losses due to trapped magnetic flux in a large-grain Nb cavity were lower than typically measured in fine-grain cavities of comparable purity and for similar temperature gradients [10]. Furthermore, experiments on SRF cavity-grade Nb samples showed that pinning in large-grain Nb is weaker than in fine-grain niobium [11]. The ability to expel flux in fine-grain cavities improved after annealing in a vacuum furnace at 900-1000 °C [12], which typically results in grain growth and reduction of density of dislocations.

Flux trapping occurs due to pinning of flexible line vortices by materials defects distributed throughout the cavity wall thickness. Yet not all of these vortices contribute to the rf losses as the rf dissipation is due to the oscillation of vortex segments in a thin layer at the surface, where the rf current flows. Figure 1 shows a schematic representation of the curved cavity surface in the equator region, where the surface magnetic field is highest, and four representative configurations of pinned vortices: normal to the surface, pinned by strong single pins or pinned collectively by array of weak pins, parallel to the surface, or pinned deeper in the bulk.

There can be multiple pinning mechanisms even in

* dhakal@jlab.org

high-purity niobium, with stronger pinning by nonsuperconducting nanoprecipitates, grain boundaries, dislocation networks and weaker collective pinning of randomly distributed impurities resulting in local variations of mean free path, δl or critical temperature, δT_c (see, e.g., a review [13]). It is known that impurities can play a major role in determining the performance of niobium SRF cavities and treatments such as low-temperature baking (LTB) [14] or doping by thermal diffusion [1, 2] allow changing the niobium properties to a depth of the order of the rf penetration depth. Such treatments could not only change the mean free path in the normal state but also the spatial distribution, density and strength of pinning centers. Experimentally, the impact of trapped vortices on the cavity surface resistance is characterized by the so-called trapped flux sensitivity, $S = R_{res}/B_{trapped}$, given by the ratio of the residual resistance divided by the magnitude of the trapped flux. Such quantity reflects the overall dissipation due to vortices trapped by different pinning centers and for different configurations, some of which are shown in Fig. 1.

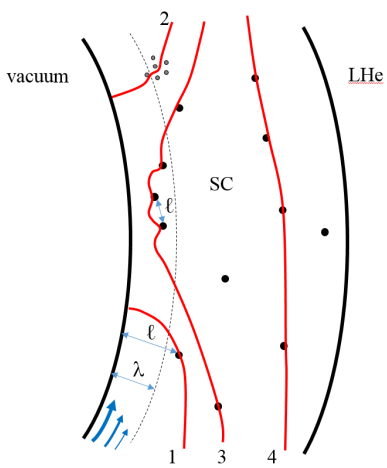

FIG. 1. A sketch of the curved cavity wall with trapped vortices in the equator region (not in scale). Dots represent pinning centers, and red lines represent flexible line vortices. The rf current flows in the inner surface layer of depth $\sim \lambda$. Vortices 1 and 2 have segments normal to the surface, 1 is pinned by one strong pin, and 2 is pinned collectively by several weak pins. Vortex 3 has two pinned segments parallel to the surface within λ. Vortex 4 is not exposed to the rf field and thus does not contribute to rf losses.

Recent studies focused on the dependence of S at low rf field ($\sim$ 20 mT) on the mean free path and the frequency [15–17] of fine-grain, high-purity elliptical cavities. In such studies, different mean free path values resulted from different annealing processes. However, such processes can also alter the pinning characteristics. The objective of this work is twofold: (i) to evaluate the low-field S-parameter in large-grain cavities with different bulk impurities concentration and structural defects to infer the ability of such impurities and defects to pin vortices and (ii) to compare the results with published data and with theoretical models of the rf dissipation of vortices pinned with different orientations with respect to the surface and with different pinning strength.

The paper is organized as follows. In Sec. II the experimental setup used for the measurements of S is described. In Sec. III we present the results of our measurements of the flux sensitivity parameter S. In Sec. IV we compare our experimental data with other data published in the literature and fit the data using different theoretical models to infer flux pinning characteristics and other important superconducting parameters. In Sec. V we discuss contributions of different pinning mechanisms to S and the effect of the mean free path on superconducting parameters which control S. Sec. VI gives the main conclusions of our work.

II. EXPERIMENTAL SETUP

Three 1.3 GHz single-cell cavities made from discs cut from ingots with different purity were used for this study. The cell shape is that of the cavities for the TESLA/XFEL project [18], cavity TC1N1 is a center-cell shape (G = 269.8 Ω), cavities G2 and KEK-R5 are end-cell shape (G = 271.6 Ω). The cavity name, ingot Nb manufacturer and main interstitial impurities for each ingot are shown in Table I.

The cavity TC1N1 and G2 were fabricated and processed at Jefferson Lab [19, 20], whereas the cavity KEK-R5 was fabricated and processed initially at KEK [21][50]. All three cavities were electropolished, removing $\sim$ 20 μm of material from the inner surface, prior to this study. The setup of the experiment is shown in Fig. 2. A Helmholtz coil of diameter $\sim$ 30 cm was used to create a uniform magnetic field around the cell. Three single-axis cryogenic flux-gate magnetometers (FGM) (Mag-F, Bartington) were mounted on the cavity surface parallel to the cavity axis in order to measure the residual magnetic flux density at the cavity outer surface during the cooldown process. Two magnetic sensors were placed at the equator, $\sim 180°$ apart, whereas one sensor was placed on the beam tube, close to the iris, to ensure the uniformity of the magnetic flux before the cooldown. The magnetic field uniformity within the cavity enclosure is $\sim \pm 1$ mG. Six calibrated temperature sensors (Cernox, Lakeshore) were mounted on the cavity: two at the top iris, $\sim 180°$ apart, two at the bottom iris, $\sim 180°$ apart, and two at the equator, close to the flux-gate magnetometers. The distance between the temperature sensors at top and bottom iris is $\sim$ 20 cm.

The measurement procedure is as follows: (i) the magnetic field was initially set below 2 mG using the field compensation coil that surrounds the vertical dewar, without any current applied to the Helmholtz coils. (ii) the standard cavity cool-down process was applied, resulting in $\sim$ 4 K temperature difference between the top and bottom iris, corresponding to a temperature gradi-

TABLE I. Purity and manufacturer of the ingots used for the fabrication of the three single-cell cavities used in this study.

Cavity Name	Nb ingot supplier	Bulk RRR	Ta (wt. ppm)	H (wt. ppm)	C (wt. ppm)	O (wt. ppm)	N (wt. ppm)
TC1N1	Ningxia, China	60	< 100	3	9	100	30
KEK-R5	CBMM, Brazil	107	~ 1034	< 10	< 30	< 30	10
G2	Tokyo-Denkai, Japan	486	~ 81	< 0.5	< 1	< 1	< 1

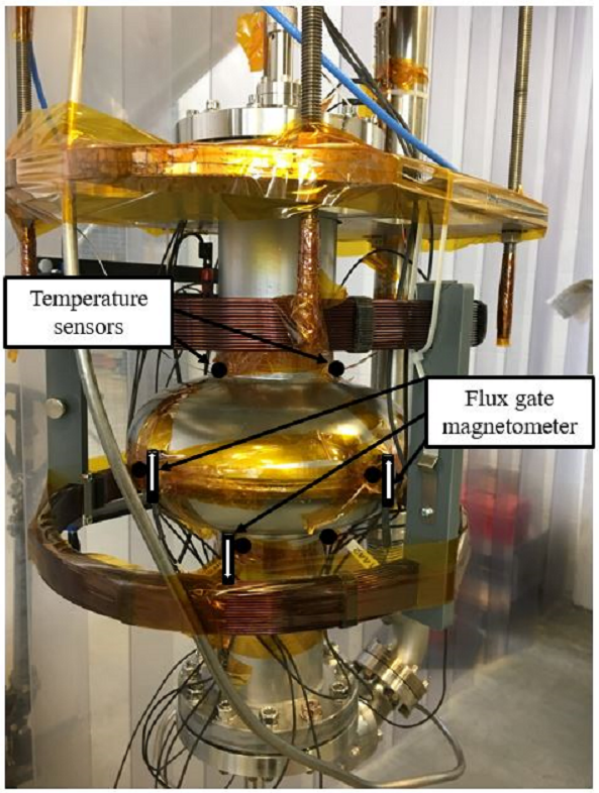

FIG. 2. Experimental set up of the single-cell cavity with Helmholtz coils, flux-gate magnetometers and Cernox sensors.

ent of ~ 0.2 K/cm. The temperature and magnetic field were recorded until the dewar was full with liquid He and a uniform temperature of 4.3 K was achieved. (iii) $Q_0(T)$ at low rf field (peak surface rf magnetic field $B_p \sim 10$ mT) from $4.3-1.5$ K was measured using the standard phase-lock technique. (iv) The cavity was warmed-up above T_c (~ 9.2 K). (v) The cavity was cooled back down to 4.3 K while keeping the temperature difference between two irises below 0.1 K and recording the temperature and magnetic field. (vi) $Q_0(T)$ from $4.3-1.5$ K was measured once more. (vi) The cavity was warmed up above T_c and the current on the Helmholtz coils is set to a certain value. Steps (ii) to (v) were repeated for three different values of magnetic field.

Fig. 3 shows the results of a magnetostatic finite element analysis using the software COMSOL [22] for a single-cell cavity of the same geometry as the one used for our experiments. A magnetic field of 10 mG was applied parallel to the cavity axis and the color map shows the distribution of the magnetic field calculated for a perfectly diamagnetic cavity, as it is expected in the ideal superconducting state. Figure 3(b) shows the ratio of the magnetic field just outside the equator in the superconducting state divided by the applied field as a function of the permeability of the cavity. Different values of permeability represent different amount of trapped magnetic field.

III. EXPERIMENTAL RESULTS

A. Cool-down and flux expulsion

The ratio of the residual dc magnetic field measured after (B_{SC}) and before (B_N) the superconducting transition qualitatively explains the effectiveness of the flux expulsion during the transition. As shown in Fig. 3, a value of $B_{SC}/B_N = 1$ represents complete trapping of magnetic field during cooldown, whereas a flux expulsion ratio of 1.7 at the equator and 0.4 at the iris would result from the ideal superconducting state. Experimentally, B_{SC}/B_N depends on the Nb material and on the temperature gradient along the cavity axis during the cool-down. Values of B_{SC}/B_N close to the theoretical estimate could be achieved with high temperature gradient ($\Delta T > 10$ K) [4, 10, 12, 15]. A representative plot of the residual magnetic field at the FGMs locations measured during one cool-down cycle for cavity G2 is shown in Fig. 4. The average value of B_{SC}/B_N for the two FGMs at the equator was 1.45 ± 0.05 and 0.35 for the FGM close to the iris. The jumps in magnetic flux density occurred at 8.9 K for sensor m1, 9.1 K for sensors m2 and 9.3 K for sensor m3. The temperature difference between the top and bottom iris when the bottom iris reached 9.2 K was 2.6 K Figure 5 shows the average flux expulsion ratio at the equator measured for the three cavities (TC1N1, KEK-R5 and G2) after removal of ~ 20 μm from the inner surface by electropolishing. All three cavities showed good flux expulsion with $B_{SC}/B_N \sim 1.5$ when the temperature difference between irises was greater than 4 K.

B. rf measurements

The average rf surface resistance was obtained from the measurement of $Q_0(T)$ at low rf field ($B_p \sim 10$ mT) for two different cool-down conditions, one with uniform

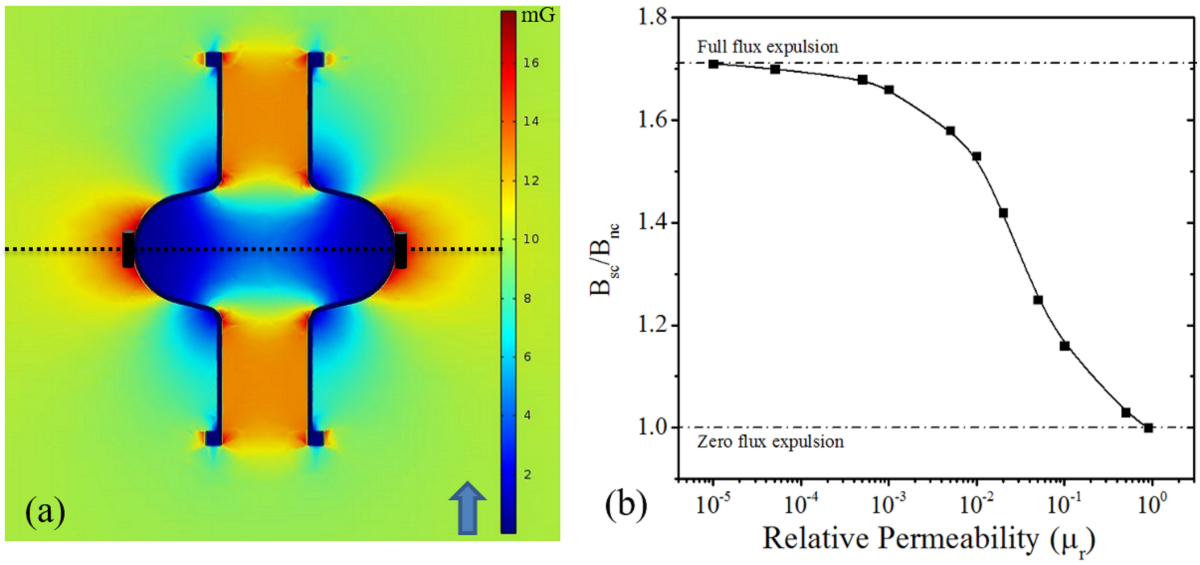

FIG. 3. (a) Contour plot of the magnetic field distribution around the perfectly diamagnetic cavity with an axial uniform magnetic field of 10 mG, shown by the arrow. (b) The flux expulsion ratio as a function of relative permeability (μ_r) of the bulk Nb at the center of the FGM at the equator.

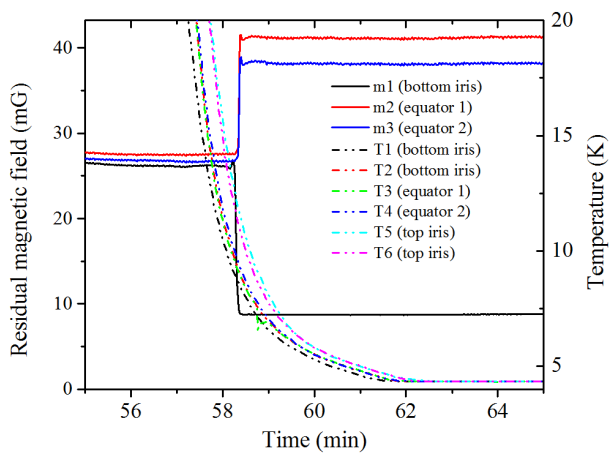

FIG. 4. Temperature and magnetic field during transition from normal to superconducting state measured during a cool-down cycle of cavity G2.

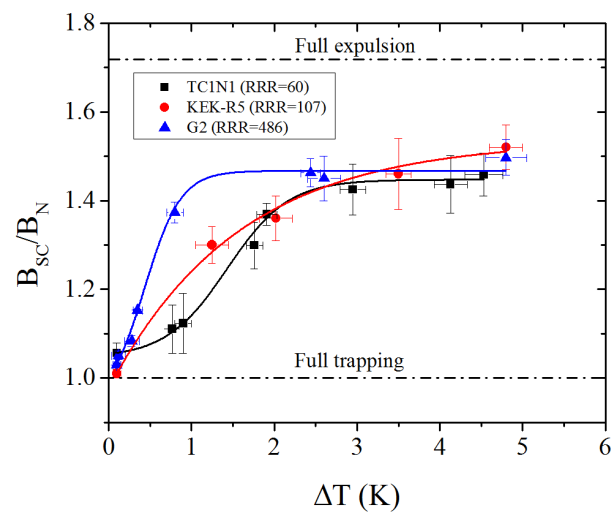

FIG. 5. Average flux expulsion ratio at the equator as a function of the temperature difference (iris-to-iris) on cavities after EP surface treatment. The lines are sigmoidal fits to the data.

temperature ($\Delta T < 0.1$ K) and one with high temperature gradient ($\Delta T > 4$ K). Such measurements were repeated with different values of applied dc magnetic field, B_a, prior to each cool-down. The $R_s(T)$ data are shown, as an example, in Fig. 6 for cavity G2. The data were fitted with the following equation:

$$R_s(T) = R_{BCS}(T, l, \Delta/k_B T_c) + R_{res} \qquad (1)$$

where R_{BCS} is the surface resistance computed numerically from the Mattis-Bardeen theory [23] and R_{res} is a temperature independent residual resistance. The mean free path, l and the ratio $\Delta/k_B T$ were considered fit parameters, where T_c is the critical temperature Δ is the energy gap at $T = 0$, and k_B is the Boltzmann constant. We took $T_c = 9.2$ K, the coherence length, $\xi_0 = 39$ nm and the London penetration depth, $\lambda_L = 32$ nm for Nb in the clean limit, $\xi_0 \ll l$ at $T = 0$. The values of residual resistance obtained from the least-squares fit of the data sets in the Arrhenius plot shown in Fig. 6 for the electropolished cavities after cool-down in low residual field (< 2 mG) and $\Delta T > 4$ K were (2 ± 0.2) nΩ for cavity G2, (0.5 ± 0.5) nΩ for cavity KEK-R5 and (3.7 ± 0.1) nΩ for cavity TC1N1. The values of l and $\Delta/k_B T_c$ did

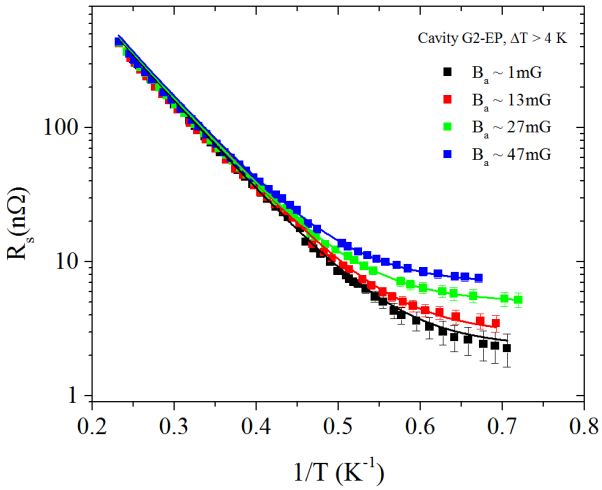

FIG. 6. $R_s(T)$ measured in electropolished cavity G2 for cool-downs with $\Delta T > 4$ K with different applied dc magnetic field values prior to cool-down. Solid lines are fits with Eq. (1).

not change, within experimental uncertainty, with different cool-down conditions or applied dc magnetic field < 50 mG. The weighted average values of l and Δ/k_BT_c from eight data sets for each cavity are shown in Table II. These mean free path values indicate that the surfaces of all three cavities were in a moderately dirty limit $l \lesssim \xi_0$. The extracted value of Δ/k_BT_c is $\sim 20\%$ lower in the low-purity cavity as compared to the other two. Since the mean free path may vary over the scale $\lesssim \lambda_L(T)$ perpendicular to the surface the temperature range used to extract l is indicated between parenthesis in Table II.

Figure 7 shows the residual resistance as a function of the applied dc magnetic field before the cavity transitions from the normal to superconducting state in the two cool-down conditions, one which leads to good flux expulsion ($\Delta T > 4$ K) and one which leads to nearly complete flux trapping ($\Delta T < 0.1$ K).

For uniform cool-down conditions, the measurements of B_{SC}/B_N indicate that nearly all the magnetic flux is trapped, therefore $R_{res}(B_a)$ can be described by Eq. (2):

$$R_{res}(B_a) = R_{res0} + SB_a, \tag{2}$$

where R_{res0} accounts for contributions to the residual resistance other than trapped flux, such as nonsuperconducting nano-precipitates, suboxide layer at the surface, broadening of the density of states [24], etc. For cool-down conditions with large ΔT, only a fraction η_t of the applied field is trapped, therefore $R_{res}(B_a)$ can be described by Eq. (3):

$$R_{res}(B_a) = R_{res0} + \eta_t SB_a. \tag{3}$$

The slope from a least-square linear fit of $R_{res}(B_a)$ for $\Delta T < 0.1$ K is the trapped flux sensitivity, whereas the fraction of the applied field which is trapped can be obtained from the slope of a least-square linear fit of $R_{res}(B_a)$ for $\Delta T > 4$ K. The values of S, R_{res0} and

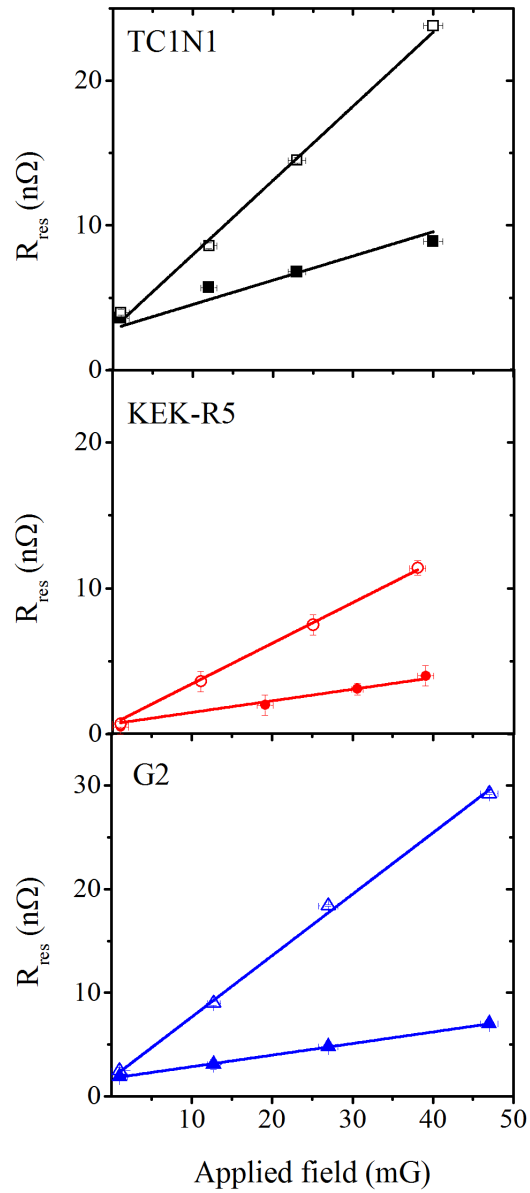

FIG. 7. Residual resistance as a function of applied dc magnetic field measured for $\Delta T < 0.1$ K (empty symbols) and $\Delta T > 4$ K at T_c (solid symbols) for the three cavities after EP surface treatment. The solid lines are linear least-squares fits to the data.

η_t are listed in Table II for the three cavities. A common value of R_{res0} was obtained by the least-square fit from the two data sets for each cool-down condition.

To explore the effect of the surface preparation on the flux expulsion and the sensitivity of R_{res} to trapped flux, the cavity G2 was re-measured after nitrogen doping. The doping procedure consisted of annealing the cavity at 800 °C for 3 hours in vacuum, followed by 2 minutes of exposure to nitrogen at pressure ~ 25 mTorr. The nitrogen was then evacuated and the cavity temperature was maintained at 800 °C for 6 minutes. The cavity was electropolished to remove ~ 7 μm from the inner

TABLE II. S, R_{res0} and fraction of the applied field being trapped, η_t, obtained from fits of $R_{res}(B_a)$ for different cool-down conditions and weighted average values of mean free path and Δ/k_BT_c obtained from fits of eight data sets of $R_s(T)$ between $1.5-4.3$ K for each cavity processed by EP.

Cavity Name	Bulk RRR	$l(1.5-4.3$ K) (nm)	Δ/k_BT_c	R_{res0} (nΩ)	S (nΩ/mG)	η_t (%)
TC1N1	60	27 ± 13	1.833 ± 0.004	2.9 ± 0.6	0.64 ± 0.06	56 ± 15
KEK-R5	107	26 ± 10	1.856 ± 0.004	0.7 ± 0.1	0.29 ± 0.01	33 ± 6
G2	486	26 ± 25	1.867 ± 0.004	1.8 ± 0.1	0.59 ± 0.01	19 ± 3

surface. Figure 8 shows B_{SC}/B_N as a function of ΔT between irises and the residual resistance as a function of the applied dc magnetic field for the two cool-down conditions. The slope of $R_{res}(B_a)$ is close to the value obtained prior to doping if the cavity is cooled in a large temperature gradient, however it increases by a factor of ~ 2 after a uniform cool-down. The least-squares fits of eight data sets of $R_s(T)$ between 1.5 K$-$4.3 K after N-doping gave the weighted average values $l = 26 \pm 25$ nm and $\Delta/k_BT_c = 1.838 \pm 0.004$.

Another treatment which affects the near-surface superconducting rf properties of niobium is the LTB. After electropolishing, the cavity KEK-R5 was baked at 120 °C for 24 hours in ultra-high vacuum and re-tested. Figure 9 shows the flux expulsion ratio as a function of ΔT and $R_{res}(B_a)$ before and after LTB. There was no significant effect of LTB on flux expulsion. After LTB the residual resistance increased to ~ 4 nΩ and the slope of $R_{res}(B_a)$ increased by $\sim 40\%$. The weighted average values of l and Δ/k_BT_c from least-squares fits of eight data sets of $R_s(T)$ between 1.5 K$-$4.3 K after LTB are (27 ± 13) nm and 1.873 ± 0.004, respectively. After this set of measurements, the cavity KEK-R5 was re-processed by annealing at 800 °C/3 h in a vacuum furnace, followed by ~ 20 μm removal by EP and LTB at 120 °C/24 h. The measurements of $R_{res}(B_a)$ were repeated and the results were within one standard deviation from the results of the previous test after LTB, providing some confidence in the reproducibility of the results.

In order to obtain information about the normal state mean free path near the surface, we measured the resonant frequency and the quality factor while warming up the cavities from ~ 5 K to ~ 10 K using a vector-network analyzer, from which $R_s(T)$ and the change in rf penetration depth $\Delta\lambda(T)$ can be obtained in this temperature region [14]. These measurements were done on cavities TC1N1 after EP, KEK-R5 after LTB and G2 after N-doping at a peak surface rf magnetic field in the range $0.03-0.3$ mT and the data are shown in Figs. 10 and 11. The data in the superconducting state were fitted using the numerical solution of Mattis-Bardeen (M-B) theory. The ratio Δ/k_BT_c was obtained from the fit of $R_s(T)$, whereas $l(7.5-9.1$ K) and T_c are weighted averages of the results from the fit of both $R_s(T)$ and $\Delta\lambda(T)$. The normal-state dc resistivity at 10 K, ρ_n, was calculated from the value of the surface resistance at 10 K using a numerical solution of the surface impedance of normal metals [26]. The value of mean free path can be calculated as follows [24]:

$$l(10\,\mathrm{K}) = \frac{\hbar\left(3\pi^2 n_0\right)^{1/3}}{n_0 e^2 \rho_n}, \tag{4}$$

where $\hbar$ is Planck constant, e is the electron charge and n_0 is the electron density. For Nb, we used $n_0 = 2.2 \times 10^{29}$ 1/m^3 or 1.6×10^{29} 1/m^3, depending on the bond path [27]. Table III lists the values of T_c, Δ/k_BT_c and l from fitting of the surface impedance in the superconducting state, as well as the surface RRR, the skin depth, δ_n, and the mean free path in the normal state at 10 K. To calculate the surface RRR, we took $\rho_n(293\text{ K}) = 14.7$ $\mu\Omega$ cm. The values of R_{res0}, S and η_t for cavities subjected to different surface treatments are listed in Table IV.

IV. COMPARISON WITH PUBLISHED DATA AND THEORETICAL MODELS

The data listed in Tables II and IV show that the fraction of magnetic field trapped during cool-down with $\Delta T > 4$ K increases with decreasing bulk RRR of the cavity and it is not significantly affected by surface treatments, such as N-doping and LTB. This rather important finding suggests that pinning is dominated by the bulk properties of the material. The grain structure is similar in all three cavities, and the major differences are in the concentration of interstitial impurities, which should be uniformly distributed in the material. On the other hand, the trapped-flux sensitivity does not seem to be correlated with the bulk RRR. This can be expected since only trapped-vortex segments at the surface contribute to rf losses. The flux sensitivity S increased by $\sim 50\%$ after LTB and $\sim 76\%$ after N-doping, showing that surface treatments significantly affect S, consistent with published data on fine-grain Nb cavities [12, 15, 16].

The normal electron mean free path is a material parameter that can be significantly altered by surface treatments. In earlier studies, l is extracted from fitting of the temperature dependent surface impedance, $Z_s(T)$, with numerical solutions of the M-B theory and it can vary depending on the depth probed by the rf current, as such depth increases rapidly above $\sim 0.85T_c$ [14]. There are many uncertainties in evaluating l by using M-B theory to fit the data given many material parameters requiring assumptions on some of those and/or computational inten-

TABLE III. Material parameters obtained from fits of $R_s(T)$ and $\Delta\lambda(T)$ between $7.5-9.2$ K with M-B theory, T_c, l and Δ/k_BT_c, along with the RRR of the surface layer, skin depth and mean free path in the normal state at 10 K for cavities of different purity and with different final surface treatment. The values of the trapped flux sensitivity and of the fraction of trapped flux are also listed in Table 3.

Cavity Name	Bulk RRR	Treatment	T_c (K)	$l(7.5-9.1)$ K (nm)	Δ/k_BT_c	Surface RRR	δ_n (nm)	$l(10$ K$)$ (nm)
TC1N1	60	EP	9.19 ± 0.06	107 ± 58	1.90 ± 0.09	50	765	133 ± 21
KEK-R5	107	LTB	9.19 ± 0.05	122 ± 74	2.0 ± 0.2	112	530	297 ± 45
G2	486	N-doping	9.24 ± 0.03	114 ± 29	1.96 ± 0.06	39	860	103 ± 16

TABLE IV. Residual resistance at zero applied dc field, the trapped flux sensitivity and fraction of trapped flux obtained for cavities with different purity and final surface treatment.

Cavity Name	Treatment	R_{res0} (nΩ	S (nΩ/mG)	η_t (%)
TC1N1	EP	2.9 ± 0.6	0.64 ± 0.06	56 ± 15
KEK-R5	LTB	3.6 ± 0.3	0.44 ± 0.02	30 ± 12
G2	N-doping	1.6 ± 0.2	1.04 ± 0.01	16 ± 7

sive grid-search methods to find a global minimum of chi-squared [28]. By contrast, obtaining the mean free path from the normal state resistivity only requires knowledge of the electron density, as shown by Eq. (4). Yet because the normal skin depth is about $3-10$ larger than the rf penetration depth at $T<0.85T_c$, measurements of the surface impedance in the normal state probes a significantly thicker surface layer of the material.

A study in which the depth profile of the magnetic field in Nb samples treated by EP and LTB was measured by muon spin rotation (μ-SR) showed that the field decay within the top ~ 100 nm is non-exponential in the LTB sample, suggesting that the material properties are changing within that depth [29]. The data was described using a Pippard/BCS non-local model and a mean free path in the range $2-16$ nm was used to fit the data. The mean free path value obtained by fitting $R_s(T)$ with the M-B theory in LTB cavities was found to be ~ 26 nm, whereas it was greater than ~ 200 nm in cavities treated by EP [14]. The values of $l(1.5-4.3$ K$)\sim 26$ nm after EP for all three cavities, as shown in Table II are lower than typical and this may be due to the cavities' treatment history. There are many uncertainties in extracting l from the low-field data by fitting $Z_s(T)$ close to T_c with M-B theory because of additional contributions to the rf losses due to a proximity coupled thin suboxide surface layer [25], common broadening of the gap peaks in the idealized BCS density of state [24], significant effects of strong electron-phonon coupling in Nb [30] or two-level systems [31] which are not taken into account in the M-B model.

Rf dissipation due to trapped vortices has been calculated both for a pinned vortex which has a segment normal to the inner cavity surface [24, 32] and for a pinned vortex which has multiple segments parallel to the inner surface [33], as illustrated by Fig. 1. Such models allow calculating the trapped flux sensitivity and its dependence on the mean free path and pinning forces. The basic equation of motion of a flexible vortex line under the action of the viscous, bending, pinning and the rf current driving forces causing the local displacement of the vortex line $u(z,t)$ along the x-axis is given by [34, 35]:

$$\eta\dot{u}=\epsilon u''-\sum_m f_p(u-x_m,z-z_m)+Fe^{-u/\lambda+i\omega t}. \quad (5)$$

Here $F=\phi_0B_p/\mu_0\lambda$ is the amplitude of a weak rf driving force, η is the viscous drag coefficient, ϵ is the vortex line tension, the overdot and the prime mean differentiation over time and the coordinate z perpendicular to the surface, respectively. Eq. (5) also includes the sum of elementary pinning forces $f_p(x-x_m,z-z_m)$ produced by materials defects located at (x_m,y_m,z_m).

Solution of the nonlinear partial differential equation (5) for either correlated or randomly-distributed pinning centers is an extremely complicated problem [34, 35]. It however, can be simplified based on the fact that pinning in Nb is weak, that is, the depinning critical current density J_c is orders of magnitude lower than J_c of superconducting materials used in magnets [13]. This suggests that pinning in the SRF materials may be produced by either dense arrays of weak materials defects or by sparse arrays of strong pins spaced by distances $\gg\lambda$. In this case calculation of the vortex dissipation can be reduced to the analysis of Eq. (5) in three distinct limiting cases: 1: A vortex segment parallel to the surface and pinned strongly by a sparse chain of materials defects spaced by ℓ; 2. A vortex segment perpendicular to the surface and pinned strongly by a materials defect spaced by ℓ from the surface. 3: A vortex perpendicular to the surface pinned collectively by randomly distributed weak defects. These cases are illustrated by Fig. 1. Calculations of the residual resistance R_{res} due to trapped vortices for these cases were done in Refs. [24, 32, 33]. The corresponding formulas for R_{res} used in the subsequent analysis of the experimental data are given in the Appendices.

In the case of weak collective pinning Eq. (5) can be simplified to the following equation for small RF vortex displacement:

$$\eta\dot{u}=\epsilon u''-\alpha u+Fe^{-x/\lambda+i\omega t}. \quad (6)$$

Here the term $-\alpha u$ describes the effect of pinning, where the Labusch spring constant α [13, 34, 35, 40] is evaluated in Appendix C for arrays of small nanoprecipitates or

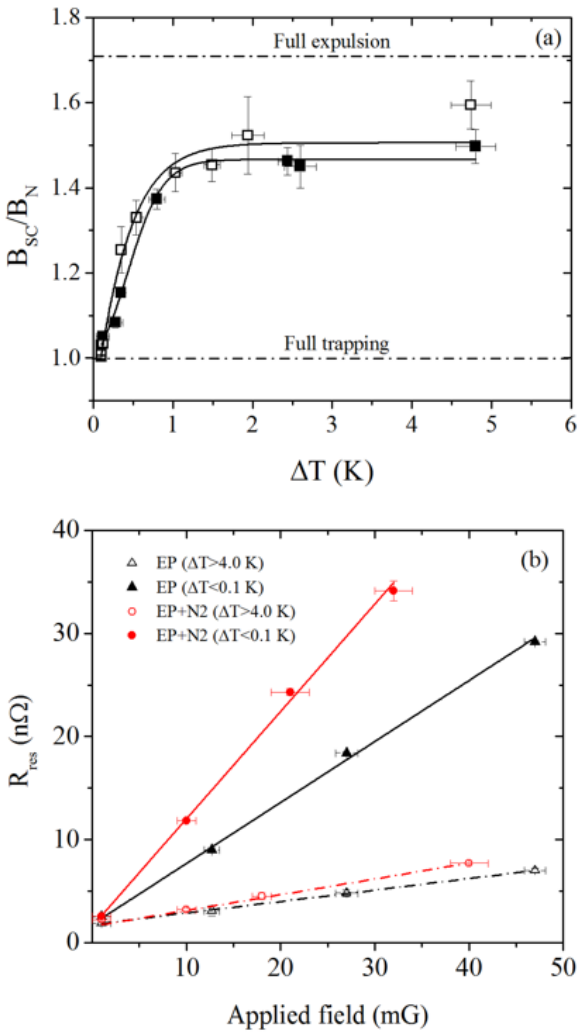

FIG. 8. (a) Flux expulsion ratio as a function of spatial temperature difference (iris-to-iris) on cavity G2 after the EP (solid symbols) and nitrogen doping (empty symbols). Solid lines are fits with a sigmoidal curve. (b) Residual resistance as a function of applied field with different surface treatments and cool-down conditions. Lines are linear least-square fits to the data.

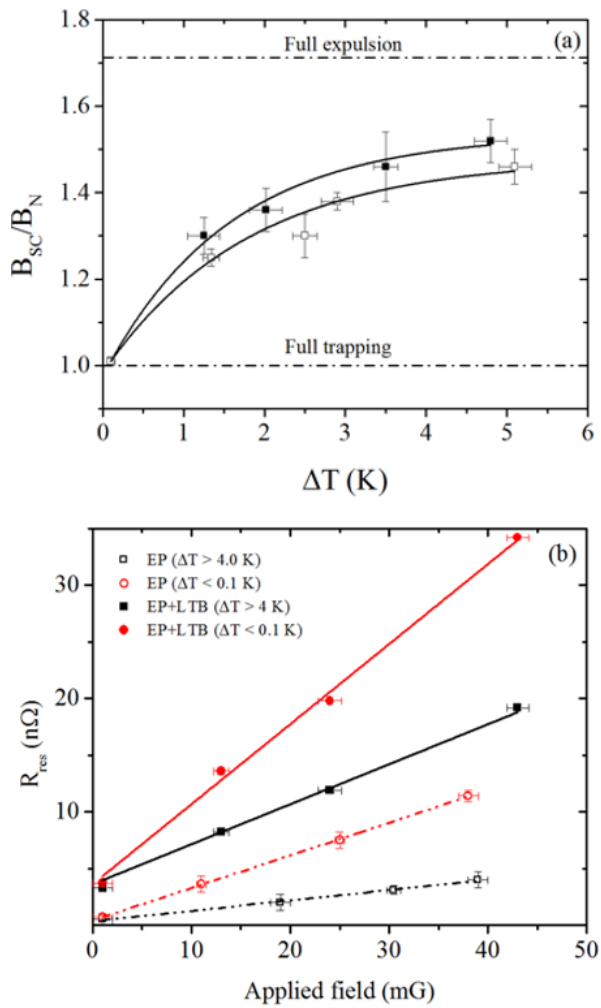

FIG. 9. (a) Flux expulsion ratio as a function of spatial temperature difference (iris-to-iris) on cavity KEK-R5 after EP (solid symbols) and LTB (empty symbols). Solid lines are fits with a sigmoidal curve. (b) Residual resistance as a function of applied field with different surface treatments and cool-down conditions. Lines are linear least-square fits to the data.

atomic impurities. As shown in Appendix C, the RF current flowing in the surface layer of thickness λ causes RF oscillations along the vortex line which extend over the Campbell penetration length L_ω given by [13, 35, 40]:

$$L_\omega = \sqrt{\frac{\epsilon}{\alpha + i\omega\eta}} \tag{7}$$

As shown in Appendices B and C for weak pinning and small α and GHz frequencies, the length L_ω can be much larger than λ. Therefore, the vortex dissipation occurs not only in the surface layer of the rf currents but also comes from long segments of trapped vortex lines extending deep inside the cavity wall over the length $\sim L_\omega$. It should be emphasized that any adequate model of pinned vortices driven by the rf current must include a finite vortex line tension ϵ, otherwise there would be no pinning [13, 34, 35]. Indeed, for infinite ϵ, the energy of a long, straight vortex does not change as it shifts through randomly distributed pins, resulting in no pinning. No pinning also happens in the opposite limit of zero ϵ, as soft vortex segments between pinning centers would simply bow out and reconnect under the Lorentz force of any infinitesimal current density. These issue is relevant to recent models of RF vortex dissipation [36, 37] in which the vortex line tension was disregarded and the Gittleman-Rosenblum (GR) model [38] was used. However, the GR model was developed to describe the dynamics of short perpendicular vortices driven by a uniform rf current in a superconducting thin film. Applying the GR pinball vortex model to long pinned vortices a bulk superconductor

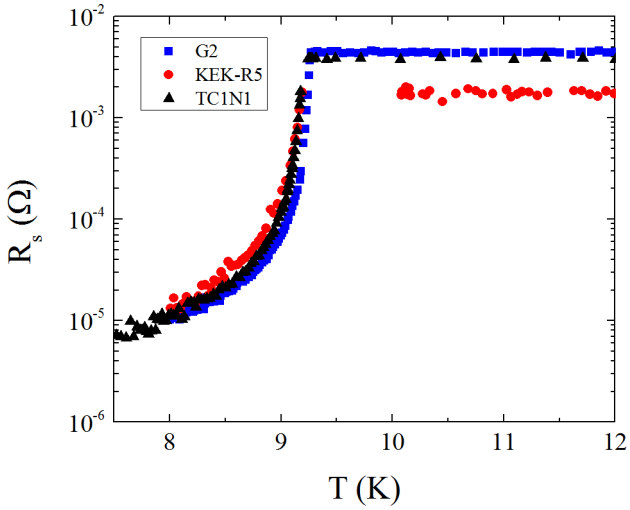

FIG. 10. Surface resistance versus temperature between 7.5 K and 12 K measured on cavity TC1N1 after EP, KEK-R5 after LTB and G2 after N-doping.

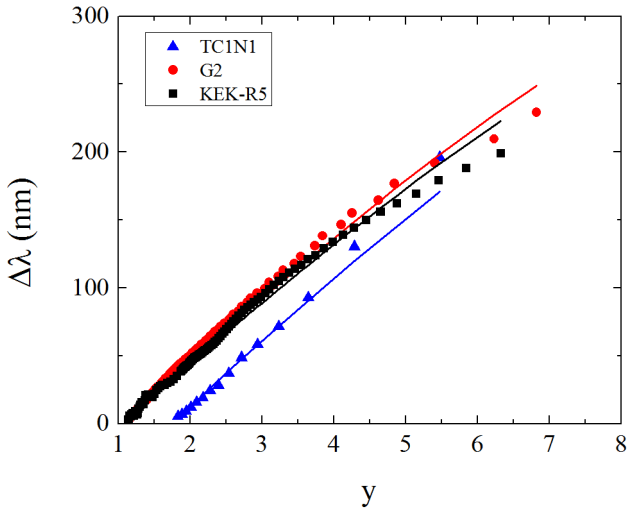

FIG. 11. Change of penetration depth as a function of the reduced temperature parameter $y = 1/\sqrt{1-(T/T_c)^4}$ measured on cavity TC1N1 after EP, KEK-R5 after LTB and G2 after N-doping. Solid lines are fit with M-B theory.

cannot give a physically adequate description of the RF power caused by trapped flux in the SRF cavities. The reason is that a vortex with either zero or infinite line tension cannot be pinned, which readily follows from the expression for α given in Appendix C which shows that α vanishes and L_ω diverges as $\epsilon \to \infty$.

The GR model may be qualitatively applicable to nearly straight perpendicular vortices in thin films [38] or SRF coatings, if the film thickness d is smaller than the pinning correlation length $L_c \simeq \xi(J_d/J_c)^{1/2}$ [39]. Here L_c defines a characteristic length of bending distortion along the vortex line in the collective theory of weak pinning [34, 35]. The applicability condition of the GR model is then:

$$d \lesssim L_c \sim \xi\sqrt{\frac{J_d}{J_c}}, \tag{8}$$

where $J_d \simeq \phi_0/4\pi\mu_0\lambda^2\xi$ is the depairing current density. For clean Nb with $\lambda \approx \xi \approx 40$ nm, we obtain $J_d \simeq 2\cdot 10^{12}$ Am^{-2}. Since Nb is a weak pinning material with $J_c \sim 10^8$ Am^{-2} [13], Eq. (8) yields $L_c \sim 6$ μm, so the GR model may be applicable to a few micron thick Nb coatings in Nb/Cu cavities. However in bulk Nb cavities L_c is much smaller than the thickness of the cavity wall $\simeq 2-3$ mm, so the GR model is no longer applicable as the line tension of the vortex must be taken into account.

In this work we focus on the dependence of vortex losses on materials parameters and RF frequency at low fields, $H_p \ll H_c \simeq 200$ mT, leaving aside a much more complicated theory of nonlinear vortex losses at high fields. Low-frequency vortex losses at high RF fields were addressed theoretically both in the limit of weak collective pinning and hysteretic depinning of vortices from strong pins [40]. Recently the theory of collective pinning was used to address the linear dependence of the vortex surface resistance on the RF field amplitude [41] observed on Nb cavities.

A. Mean free path dependence

Measurements of trapped flux sensitivity as a function of mean free path have been done on fine-grain, 1.3 GHz cavities made of high-purity Nb and of the same shape as that of our study have been reported in Refs. 15 and 16. In Ref. 16 fifteen different cavities were subjected to different annealing followed by EP. In Ref. 15 six different cavities were subjected to different annealing followed by different amount of material removal by EP. The S-values published in Ref. 15 had to be multiplied by a correction factor of 0.58 to be compared with the data from Refs. 16 and 17 and that from our work [42] The data from Refs. 15 and 16 are shown along with our data in Figs. 12-14. Figure 12 shows the calculated S for a vortex parallel to the surface pinned by a periodic chain of pins of strength $\zeta = 20$, defined in Appendix B 1, and different values of pins spacing ℓ. The calculation gives a peak in the $S(l)$ curve at $l \sim 10$ nm if the pin-spacing is proportional to l, as it was proposed in [15]. Such assumption might be justified in case pinning is cause by precipitates which also act as electrons' scattering centers.

Figure 13 shows the calculated S for a vortex normal to the surface for different values of the pin distance from the surface. Figure 14 shows the calculated S for a vortex normal to the surface for the case of weak collective pinning due to δT_c variations, for different values of the pinning parameter $\alpha_p = 4\pi\lambda_0^2\alpha_0/\Phi_0^2$, where α_0 is defined in Appendix C. The Bardeen-Stephen model was used for the vortex viscosity $\eta(l)$ in all the calculations, however, this model is valid only in the dirty limit. Similar mean free path dependence of $\eta(l)$ to the Bardeen-

Stephen model can be expected in the moderate clean limit, although with a different scaling factor, as it is explained in Appendix A. Therefore, a discrepancy between the experimental data and the calculations can be expected in the moderate clean limit. The results from the calculations with the various models are shown as dashed lines in Figs. 12-14 for $l > 100$ nm, as there is no well-established theory of $\eta(l)$ in the clean limit.

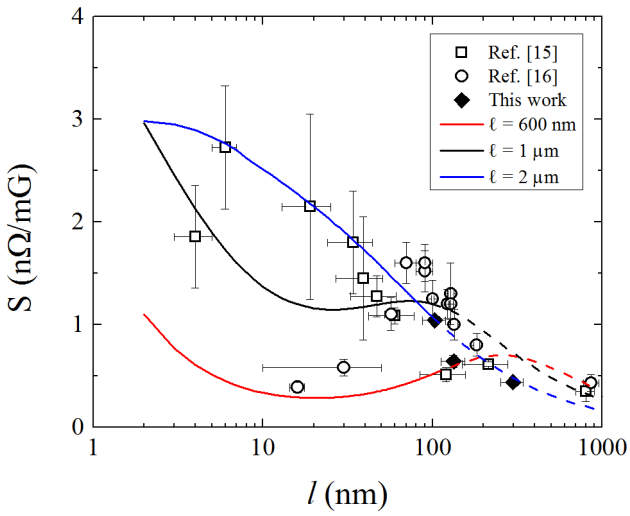

FIG. 12. Trapped flux sensitivity as a function of mean free path. Solid lines are calculated for the case of a vortex parallel to the surface pinned by a periodic chain of pins of strength $\zeta = 20$ and with spacing ℓ (a). Dashed lines are extrapolations to the clean limit.

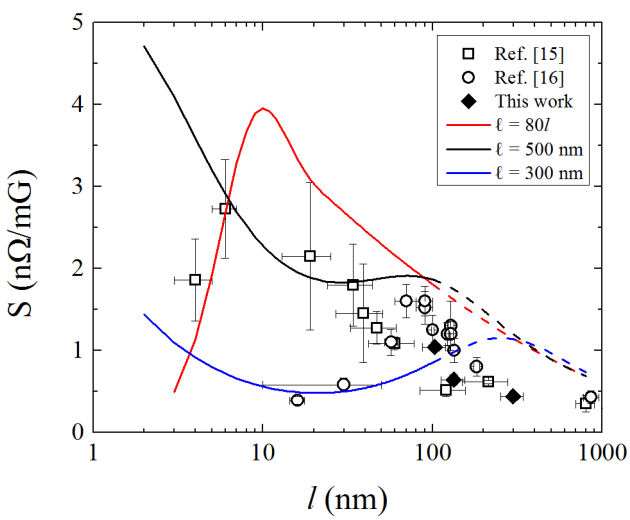

FIG. 13. Trapped flux sensitivity as a function of mean free path. Solid lines are calculated for the case of a vortex normal to the surface for different values of the pins distance from the surface, ℓ. Dashed lines are extrapolations to the clean limit.

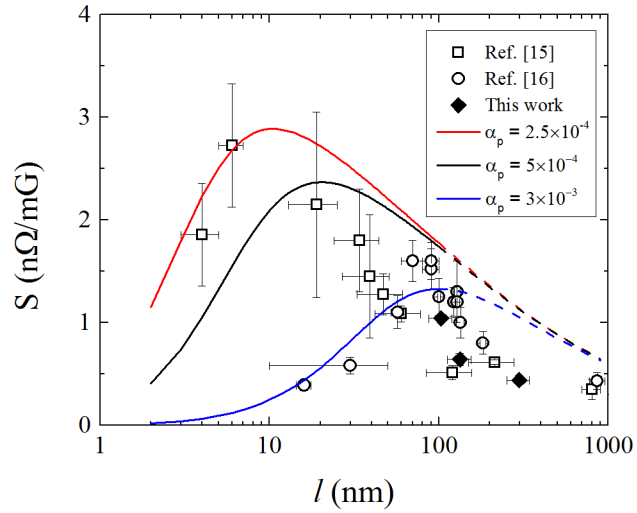

FIG. 14. Trapped flux sensitivity as a function of mean free path. Solid lines are calculated for the case of a vortex normal to the surface for the case of weak collective pinning for different values of the pinning parameter α_p. Dashed lines are extrapolations in the clean limit.

B. Frequency dependence

Figures 15-17 show the trapped flux sensitivity normalized to the high-frequency limit $S_n = S/S_{hf}$ as a function of the normalized frequency $\chi = \omega/\omega_\lambda$, where $\omega_\lambda = \epsilon/\eta\lambda^2$ is a characteristic oscillation frequency of the vortex segment [33] at which $L_\omega \sim \lambda$ and vortex dissipation is localized in the rf layer. The data from Refs. 15–17 are plotted along with the data from this work and results from calculations for a vortex strongly pinned either perpendicular or parallel to the surface or for a weakly pinned vortex perpendicular to the surface. Formulae for the high-frequency limit of the trapped flux sensitivity are given in the Appendices. Since χ depends on mean-free path, cavities resonating at the same frequency but with different mean free path values result in different χ-values. Whereas most of the data shown in Figs. 15-17 are for 1.3 GHz cavities, there are also three data points each for 650 MHz, 2.6 GHz and 3.9 GHz elliptical cavities [17]. It should be pointed out that in Refs. [16, 17] the mean free path of cavities which were LTB was not obtained from cavity measurements after LTB but the same value $l = 16$ nm was arbitrarily assigned, based on data extracted from μ-SR measurements on Nb coupons. This assumption contributes to the scatter noticeable among the data.

V. DISCUSSION

The data shown in Sec. III B suggest a correlation between the fraction of trapped flux and the bulk purity of the material. Lower material purity can result in a larger

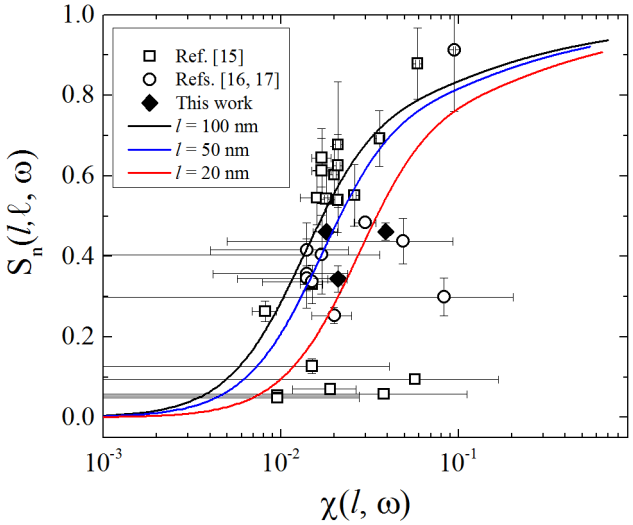

FIG. 15. Normalized trapped flux sensitivity as a function of the reduced frequency χ. Solid lines are calculated for the case of a vortex parallel to the surface pinned by a periodic chain of pins of strength $\zeta = 20$ and with spacing $\ell = 1$ μm, for different values of mean free path l (a).

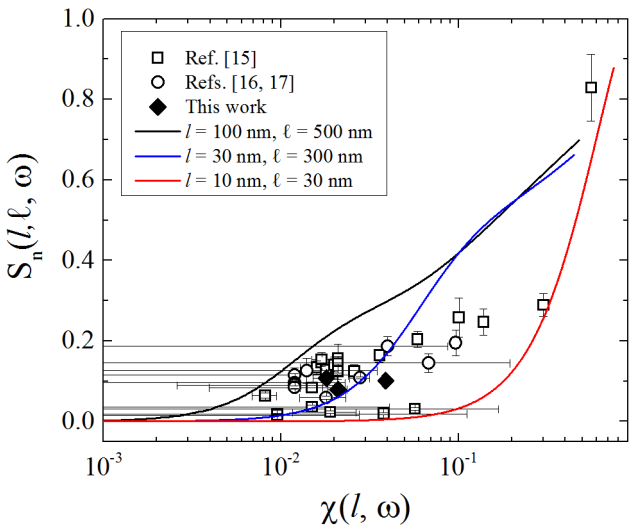

FIG. 16. Normalized trapped flux sensitivity as a function of the reduced frequency χ. Solid lines are calculated for the case of a vortex normal to the surface for different values of the pin distance from the surface, ℓ and different values of mean free path l.

fraction of the trapped flux because the vortex line tension $\epsilon \simeq \epsilon_0(1+\xi_0/l)^{-1}$ decreases as l decreases, therefore making it easier for a vortex to be pinned. While the surface RRR is similar to the bulk value for the low-purity cavity after EP and the medium purity cavity after LTB, it is much smaller than the bulk value for the high-purity cavity after N-doping. This suggests that the diffusion of N during the infusion process occurs over a depth of the order of the skin-depth ~ 1 μm in this case. This result

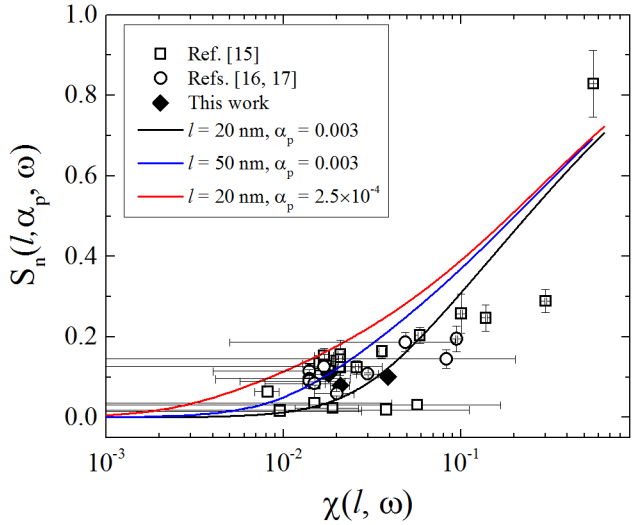

FIG. 17. Normalized trapped flux sensitivity as a function of the reduced frequency χ. Solid lines are calculated for the case of a vortex normal to the surface for the case of weak collective pinning for different values of the pinning parameter α_p and mean free path l.

is consistent with measurements of the impurities depth profile in N-doped Nb samples [43, 44].

A comparison of our data with published data on the trapped flux sensitivity as a function of the mean free path and the reduced frequency show a significant scatter among all data, which may be due to multiple reasons. One of them is the inability to accurately determine the mean free path for nonuniform distribution of impurities within the top ~ 40 nm surface layer as discussed in Sec. III B. Another possible source for the scatter in the data is due to the measurements being made on many different cavities, each with its characteristic distribution of defects within the bulk and closer to the surface, leading to many different possible distributions of trapped vortices. The data from Refs. [15, 16] may indicate the presence of a peak of $S(l)$ but the position of such peak is quite different between the two sets of data. Furthermore, analyzing $S(l)$ as a function of only the mean free path may be misleading as different heat treatments used to change l can also change distribution and strength of pinning centers, such as clusters of impurities and oxide nanoprecipitates.

Results from calculations of the mean free path and frequency dependencies of S using different models of trapped vortex configuration and pinning, shown in Figs. 12-17, provide a good qualitative description of the data with reasonable values of ℓ. The available data does not allow for any conclusion on whether a particular configuration of trapped vortices or type of pinning is prevalent. It should be emphasized that, given the randomness of the distribution of pinning center in the cavity wall, the overall trapped flux sensitivity measured for a cavity would result most likely from distributions of ℓ-values,

pinning strengths and positions of vortex segments relative to the surface. Including all these variables into a single model would result in many more fit parameters which would allow describing any possible data set.

Another complication is due to the many possible pinning mechanisms, resulting in different $S(l,\omega)$-dependencies, such as pinning from nanoprecipitates, $\delta\ell$, δT_c, or dislocation networks. In the case of weak collective pinning, the mean free path dependence of the Labusch constant for pinning due to $\delta\ell$ and δT_c variations is given in Appendix C. Ideally, it would be preferrable to investigate the mean free path and frequency dependence of the trapped flux sensitivity on the same cavity, to eliminate variabilities in the Nb material. However, the method typically used to modify the mean free path is the diffusion of interstitial impurities at temperatures above 100°C which has been shown to already change the distribution of defects, such as vacancies, in the material [45, 46]. Different pinning mechanisms and configurations of pinned vortex segments could result from changes in defects' distribution.

VI. CONCLUSION

The results of measurements of flux trapping and trapped flux sensitivity of large-grain cavities made for Nb ingots with different content of interstitial impurities suggest that the fraction of trapped flux increases with decreasing purity of the material and it is insensitive to surface treatments. On the other hand, the trapped flux sensitivity depends on the surface conditions such as the local mean free path and distribution of pinning centers.

The analysis of published data on the mean free path and frequency dependencies of the low-field trapped flux sensitivity obtained on elliptical cavities show a significant scattering in the data, which highlight the complexity of measuring such dependencies due to the many factors which play a role in determining how vortices are pinned. Such factors are statistical in nature and can be geometric, such as the position of a trapped vortex segment relative to the surface, or related to the type and strength of pinning centers.

Some of the models found in the literature describe the mean free path and frequency dependencies of S based on the Gittleman-Rosenblum which treats a flexible vortex line like a particle. While the G-R model adequately describes short perpendicular vortices in thin films for which it was originally proposed, the G-R model disregards the essential physics of RF vortex losses in a bulk SRF cavity because it neglects the key effect of a finite vortex line tension without which a long vortex threading the cavity wall cannot be pinned.

ACKNOWLEDGMENTS

We would like to acknowledge Jefferson Lab technical staff for the cavity surface processing and cryogenic support. We thank Dr. Rongli Geng for providing the cavity G2 and Dr. Ganapati Myneni and Dr. Kensei Umemori for providing the cavity KEK-R5. We also thank Dr. Mattia Checchin for providing the data in Ref. 17 and Dr. Matthias Liepe for providing us with the correction factor for the data in Ref. 15. This manuscript has been authored by Jefferson Science Associates, LLC under U.S. DOE Contract No. DE-AC05-06OR23177. The work of A. G. was supported by NSF under grant PHY 100614-010.

Appendix A: Dependencies of superconducting parameters on the mean free path

Here we summarize dependencies of superconducting parameters on the mean free path used in our fitting of the experimental data. At $T \ll T_c$ the BCS theory gives an analytical formula λ as a function of l caused by scattering on nonmagnetic impurities [24]. A popular approximation of this formula is:

$$\lambda = \lambda_0 \left(1 + \frac{\tilde{\xi}_0}{l}\right)^{1/2} \tag{A1}$$

In turn, the coherence length ξ can be approximated by

$$\xi = 0.74\xi_0 \left(1 + \frac{\tilde{\xi}_0}{l}\right)^{-1/2}, \tag{A2}$$

where $\tilde{\xi}_0 = 0.88\xi_0$. Notice that the product $\xi\lambda$ is independent of l which is a consequence of the Anderson theorem, according to which the thermodynamic critical field B_c is independent of l caused by scattering on nonmagnetic impurities. At $T \approx T_c$, this also follows from the GL result $B_c = \phi_0/2^{3/2}\lambda\xi$, whereas at $T = 0$ the BCS theory gives

$$B_c(0) = (\mu_0 N_n)^{1/2}\Delta_0, \tag{A3}$$

where $N_n = m^2 v_F/2\pi^2\hbar^3$ is the normal density of states, and Δ_0 is the superconducting gap at $T = 0$ which is also independent of l. Here $\xi_0 = \hbar v_F/\pi\Delta_0$ and $\lambda_0 = (m/\mu_0 n e^2)^{1/2}$ are the clean limit values of ξ and λ at $l \gg \xi_0$, where v_F is the Fermi velocity, m is the effective electron mass, and n is the electron density.

Consider now the vortex drag coefficient $\eta = \phi_0^2/2\pi\xi^2\rho_n$ of the Bardeen-Stephen model in which the vortex core is regarded as a normal cylinder of radius ξ and a bulk resistivity ρ_n. This implies that the mean free path is smaller than the core diameter, $l \lesssim \sqrt{l\xi_0}$, that is, the Bardeen-Stephen formula is only applicable in the dirty limit $l \ll \xi_0$. Substituting Eq. (A2)

into $\eta = \phi_0^2/2\pi\xi^2\rho_n$ and using the Drude formula for $\rho_n = p_F/ne^2l$, we get;

$$\eta \simeq \frac{\pi^2\hbar n\Delta}{4E_F}\left(\frac{l}{\xi_0}+1\right), \tag{A4}$$

where p_F and E_F are the Fermi momentum and energy. Thus, η is independent of l in the dirty limit. Yet the Bardeen-Stephen model has been used in many works to describe moderately clean superconductors $l \gtrsim \xi_0$ for which Eq. (A4) is not really applicable. Microscopic calculations of η in a moderately clean limit give [47]

$$\eta \simeq \frac{\phi_0^2}{8\pi\xi^2\rho_n}\ln\frac{\Delta}{k_BT} \tag{A5}$$

Here η exhibits a linear dependence on l similar to that of Eq. (A4) but differs by a factor $\simeq 0.25\ln(\Delta/k_BT)$ from the Bardeen-Stephen formula. Thus, using the Bardeen-Stephen model in the moderately clean limit $l \gtrsim \xi_0$ disregards a factor which can be essential when fitting the experimental data.

Appendix B: Trapped flux sensitivity formulae

Here we summarize the formulae for $S = R_{res}/B_0$ obtained by solving the dynamic equation for a flexible vortex line driven by weak rf surface current and interacting with pinning centers. It should be emphasized that taking the vortex line tension into account is instrumental for correct calculations of R_{res}. Ignoring the vortex tension and regarding trapped vortex lines as particle [36], adopting the model originally suggested to describe short perpendicular vortices in thin films [38], gives an inadequate description of vortex dissipation in the SRF cavities.

The formulae for R_{res} depend on the mutual orientation of the vortex segment with respect to the cavity surface, so we consider here three characteristic cases representing trapped vortex configurations shown in Fig. 1. In all cases, the normal state resistivity used in the calculation of η is given by Eq. (4): $\rho_n = (3.85\times10^{-10}\mu\Omega\,\mathrm{m}^2)/l$.

1. Pinned vortex parallel to the surface.

A vortex parallel to the surface under weak rf field is described by the following dynamic equation [33]:

$$\eta\dot{u} = \epsilon u'' + Fe^{-u/\lambda+i\omega t} - \frac{\phi_0^2}{2\pi\mu_0\lambda^3}K_1\left(\frac{2u}{\lambda}\right) + \sum_m f_p(u, z-m\ell_p), \tag{B1}$$

where $u(z,t)$ is a local displacement of the vortex line, η is the vortex drag coefficient, $F = \phi_0B_p/\mu_0\lambda$, $f_p(x,z)$ is an elementary pinning force, $K_1(x)$ is a modified Bessel function, and the prime and overdot denote partial derivatives with respect to z and t. The term $\epsilon u''$ describes bending distortions of the vortex line, where ϵ is a vortex line tension

$$\epsilon \simeq \frac{\phi_0^2}{4\pi\mu_0\lambda^2}\left(\ln\frac{\lambda}{\xi}+0.5\right) \tag{B2}$$

This formula defines ϵ for bending distortions with long wavelengths $\lambda \gtrsim \lambda$. A general case of both long and short wave distortions for which $\epsilon(\lambda)$ becomes dependent on λ was considered in Ref. 32.

Solution of Eq. (B1) for a vortex pinned by a periodic array of defects spaced by ℓ along z and by d from the surface gives the following formula for R_{res} [33]:

$$R_{res} = \frac{\phi_0^2\langle e^{-2d/\lambda}\rangle}{\lambda^2\eta a}\Gamma(\sqrt{\nu}), \tag{B3}$$

Here a is a mean spacing between pinned vortices, $\langle ...\rangle$ means averaging over the vortex positions d in the direction perpendicular to the surface, and

$$\Gamma(\sqrt{\nu}) = 1 - \frac{\sinh\sqrt{\nu}+\sin\sqrt{\nu}}{\sqrt{\nu}\big(\cosh\sqrt{\chi}+\cos\sqrt{\nu}\big)}, \tag{B4}$$

$$\nu = \omega\tau_p, \qquad \tau_p = \eta\ell^2/2\epsilon. \tag{B5}$$

Here τ_p is a pinning relaxation time constant. In order to calculate S, the average $\langle e^{-2d/\lambda}\rangle$ can be approximated as $e^{-2d_m/\lambda}\lambda/a$ where d_m is the minimum distance from the surface for which a vortex can be pinned. For identical pins, d_m is obtained from the numerical solution of the balance equation between the pinning force and the image force:

$$\frac{\phi_0^2}{2\pi\mu_0\lambda^3}K_1\left(\frac{2d_m}{\lambda}\right) = \frac{f_p}{\ell}, \tag{B6}$$

where the following expression is used for the pinning force:

$$f_p = \zeta\mu_0\pi H_c^2\xi^2. \tag{B7}$$

H_c is the thermodynamic critical field and ζ is a parameter used to qunatify the strength of the pins. Since $B_0 = \Phi_0/a^2$, we obtain the following expression for S:

$$S \sim \frac{\phi_0 e^{-2d_m/\lambda}}{\lambda\eta}\Gamma(\sqrt{\nu}). \tag{B8}$$

In the high-frequency limit, $\nu \gg 1$, $\Gamma(\sqrt{\nu}) \to 1$.

2. Vortex perpendicular to the surface. Sparse strong pins.

Dynamics of a perpendicular vortex segment of length ℓ pinned by a defect spaced by $z = \ell$ from the surface is described by the equation:

$$\eta\dot{u} = \varepsilon u'' + F\exp(-z/\lambda + i\omega t), \tag{B9}$$

with the boundary condition $u(\ell,t)=0$ and $u'(0,t)=0$. The surface resistance is given by [32]:

$$R_{res}=\frac{B_0\phi_0\chi^2}{2\eta\lambda}\left[\frac{5+\chi^2}{(1+\chi^2)^2}-\frac{2}{\chi^{3/2}}\mathrm{Im}\frac{\tanh\sqrt{i\nu}}{\sqrt{i}(1-i\chi)^2}\right], \tag{B10}$$

$$\chi=\frac{\omega\eta}{\varepsilon}\lambda^2, \qquad \nu=\frac{\omega\eta}{\varepsilon}\ell^2. \tag{B11}$$

In the high-frequency limit, $\chi\gg 1$, we obtain:

$$S_{hf}=\frac{\Phi_0}{2\eta\lambda}. \tag{B12}$$

As follows from Eq. (B9), the rf bending disturbance extends along the vortex line over the ripple length

$$L_\omega=(\epsilon/\eta\omega)^{1/2}=\frac{\xi}{2\lambda}\sqrt{\frac{g\rho_n}{\pi\mu_0 f}}, \tag{B13}$$

where $g=\ln(\lambda/\xi)+1/2$, f is the rf frequency and we used $\eta=\phi_0^2/2\pi\xi^2\rho_n$. For clean Nb with $\lambda\approx\xi$, $\rho_n=0.2\ \mu\Omega$ m, we have $L_\omega\simeq 130$ nm at 2 GHz. Here L_ω is practically independent of T and decreases as the m.f.p. decreases. For instance, in the dirty limit, $\lambda\simeq\lambda_0(\xi_0/l)^{1/2}$ and $\xi\simeq\sqrt{\xi_0 l}$, we have $L_\omega^{dirty}\simeq L_\omega^{clean}\sqrt{l/\xi_0}$.

Since the amplitude of the rf ripples along the vortex line decreases exponentially over the length L_ω, pins spaced by $\ell\gtrsim L_\omega$ from the surface have no effect on R_{res}, whereas pins closer to the surface reduce R_{res}. For small pins of radius $r_0<\xi$, the detailed behavior of the elementary pinning force $f_p(u)$ does not affect R_{res} which is dominated by dissipative oscillations of free vortex segments between the pins. Thus, free vortex segments of length $\ell>L_\omega$ perpendicular to the surface produce the largest rf power independent of pinning. The rf power in the vortex hotspots is determined by statistical averaging of R_{res} over the length of vortex segments [32, 33] resulting from the actual distribution of the pinning centers at a particular part of the cavity surface:

$$\bar{R}_{res}=\int_0^\infty G(\ell)R_{res}(\ell)d\ell, \tag{B14}$$

where $G(\ell)$ is a distribution function of the pin spacings.

3. Vortex perpendicular to the surface. Weak collective pinning.

Consider a vortex line interacting collectively with many weak pinning centers spaced by distances much smaller than λ. In this case the dynamic equation for the vortex perpendicular to the surface takes the form:

$$\eta\dot{u}=\varepsilon u''-\alpha u+F\exp(-z/\lambda+i\omega t), \tag{B15}$$

where the Labusch spring constant α describes the averaged effect of pinning [34] as discussed in Appendix C. The solution of Eq. (B15) which satisfies the boundary condition $u'=0$ at $z=0$ is:

$$u(z,t)=\frac{H_p\phi_0 e^{i\omega t}}{\alpha\lambda^2-\epsilon+i\omega\eta\lambda^2}\left(\lambda e^{-z/\lambda}-\lambda_c e^{-z/\lambda_c}\right). \tag{B16}$$

Here λ_c is the complex, frequency-dependent Campbell penetration depth [13, 34, 40] which defines the ripple length of the elastic vortex line disturbed by the RF current:

$$\lambda_c=\left(\frac{\epsilon}{\alpha+i\omega\eta}\right)^{1/2}=\frac{\lambda}{\sqrt{k+i\chi}}, \tag{B17}$$

where $k=\alpha\lambda^2/\epsilon$ is the pinning parameter. At $\omega=0$, Eq. (B17) defines the pinning correlation length $L_c=(\epsilon/\alpha)^{1/2}$ along a single vortex. For weak pinning $k\ll 1$ and low frequencies $\chi=\omega\lambda^2\eta/\epsilon\ll 1$, the Campbell length is much larger than λ. The surface resistance calculated using Eq. (B16) is given by [24]:

$$R_{res}=-\frac{2\pi B_0\mu_0\lambda^3\omega}{\phi_0 g}\mathrm{Im}\left[\frac{s+2}{s(s+1)^2}\right], \tag{B18}$$

where $s=\lambda/\lambda_c=\sqrt{k+i\chi}$.

In the high-frequency limit, $\chi\gg 1$, the trapped flux sensitivity is given by:

$$S_{hf}=-\frac{2\pi\mu_0\lambda^3\omega_\lambda}{\phi_0 g}. \tag{B19}$$

Appendix C: Evaluation of the Labusch constant

We evaluate α in Eq. (B15) using the standard qualitative arguments of the collective pinning theory [34] for randomly-distributed weak pinning centers, for example small dielectric nanoprecipitates of radius $r_0<\xi$ producing the maximum elementary pinning energy $u_p\sim 4\pi B_c^2 r_0^3/3\mu_0$. The pinning correlation length L_c is determined by the condition that the elastic bending energy of a vortex segment of length L_c is of the order of the pinning energy $u_p\sqrt{N}$ determined by the fluctuation number of pins within the interaction volume $r_p^2 L_c$. Here $N\sim n_p r_p^2 L_c$, where n_p is the volume density of pins and $r_p\sim\xi$ is a pin interaction radius which also defines characteristic displacements of the vortex line:

$$\epsilon\frac{r_p^2}{L_c}\sim(n_p L_c r_p^2)^{1/2}u_p. \tag{C1}$$

Hence,

$$L_c\sim\left(\frac{\epsilon\xi}{u_p\sqrt{n_p}}\right)^{2/3}, \qquad u_p\simeq\frac{4\pi r_0^3 B_c^2}{3\mu_0}. \tag{C2}$$

Comparing Eq. (C2) with $L_c=(\epsilon/\alpha)^{1/2}$ expressed in terms of the Labusch constant α, yields

$$\alpha\sim\frac{u_p^{4/3}n_p^{2/3}}{\xi^{4/3}\epsilon^{1/3}} \tag{C3}$$

To see the dependence of α on the m.f.p., we notice that u_p is independent of l because of the Anderson theorem, whereas $\epsilon = \phi_0^2 g/4\pi\mu_0\lambda^2 = \epsilon_0(1+\tilde{\xi}_0/l)$, and $\xi \simeq \xi_0(1+\tilde{\xi}_0/l)^{-1/2}$, where $\tilde{\xi}_0 \approx 0.88\xi_0$. Thus,

$$\alpha = \alpha_0\left(1+\frac{\tilde{\xi}_0}{l}\right), \tag{C4}$$

where the subscript 0 corresponds to the respective parameters in the clean limit, $l \gg \xi_0$.

The above contribution to α comes from δT_c pinning caused by small precipitates of reduced (or zero) T_c. Another contribution to α comes from $\delta\ell$ pinning resulting from statistical fluctuations of the m.f.p. of single atomic impurities. The expression for α is obtained in the same way as Eq. (C3) with the replacement of the density of nanoprecipiates $n_p \to n_i$ to the density of impurities n_i and the elementary pinning energy at $T \approx T_c$ [34, 48, 49]

$$u_p \simeq \frac{4\pi B_c^2}{3\mu_0} r_i^3, \qquad r_i \sim (G\xi_0\sigma_0)^{1/3}. \tag{C5}$$

Here the effective pin interaction radius of a single impurity r_i depends on the scattering cross-section on impurity σ_0 [48] related to l and n_i by $\sigma_0 n_i = l^{-1}$. The parameter $G = -\chi'(\xi_0/l)/\chi(\xi_0/l)$, and $\chi'(x)$ is a derivative of the Gor'kov impurity function [34]

$$\chi(x) = \sum_{n=0}^{\infty} \frac{1}{(2n+1)^2(2n+1+x)}, \tag{C6}$$

$$G(\xi_0/l) \approx \frac{1}{1+\tilde{\xi}_0/l}. \tag{C7}$$

Using Eq.(C3), (C5), we obtain α for the δl pinning:

$$\alpha \sim \frac{u_p^{4/3} n_i^{2/3}}{\xi^{4/3}\epsilon^{1/3}} \tag{C8}$$

Using here Eqs. (C5)-(C7) and $n_i = 1/\sigma_0 l$ yields the dependence of α_i on l:

$$\alpha_i = \frac{\alpha_{i0}(\tilde{\xi}_0/l)^{2/3}}{(1+\tilde{\xi}_0/l)^{1/3}}, \tag{C9}$$

$$\alpha_{i0} \simeq \left(\frac{4\pi B_c^2}{3\mu_0}\right)^{4/3} \frac{\sigma_0^{2/3}}{\xi_0^{2/3}\epsilon_0^{1/3}} \tag{C10}$$

As follows from Eqs. (C4) and (C9), δT_c and δl pinning result in different dependencies of α_i on the m.f.p. Here δl pinning becomes ineffective in the clean limit $l \gg \xi_0$ and gives a weaker dependence of $\alpha \propto l^{-1/3}$ on l than $\alpha \propto l^{-1}$ for δT_c pinning in the dirty limit. Yet α_i can exceed α in the dirty limit if

$$\frac{\sigma_0^2 n_i}{(\xi_0^{-1}+l^{-1})^2} \gtrsim r_0^6 n_p \tag{C11}$$

Here the impurity scattering length $\sim \sqrt{\sigma_0}$ is of the order of atomic size, so that $\sqrt{\sigma_0} \ll r_0 < \xi_0$, but the volume density of impurities n_i can be much larger than the volume density of nanoprecipitates, $n_p \ll n_i$. The Labusch constant for strong pinning caused by different types of defects was evaluated in Ref. 40.

[1] P. Dhakal, G. Ciovati, G. R. Myneni, K. E. Gray, N. Groll, P. Maheshwari, D. M. McRae, R. Pike, T. Proslier, F. Stevie, R. P. Walsh, Q. Yang, and J. Zasadzinzki, Effect of high temperature heat treatments on the quality factor of a large-grain superconducting radio-frequency niobium cavity, Phys. Rev. ST Accel. Beams **16**, 042001 (2013).

[2] A. Grassellino, A. Romanenko, D. Sergatskov, O. Melnychuk, Y. Trenikhina, A. Crawford, A. Rowe, M.Wong, T. Khabiboulline, and F. Barkov, Nitrogen and argon doping of niobium for superconducting radio frequency cavities: a pathway to highly efficient accelerating structures, Supercond. Sci. Technol. **26**, 102001 (2013).

[3] J.-M. Vogt, O. Kugeler, and J. Knobloch, Impact of cool-down conditions at T_c on the superconducting rf cavity quality factor, Phys. Rev. ST Accel. Beams **16**, 102002 (2013).

[4] A. Romanenko, A. Grassellino, O. Melnychuk, and D. A. Sergatskov, Dependence of the residual surface resistance of superconducting radio frequency cavities on the cooling dynamics around T_c, J. Appl. Phys. **115**, 184903 (2014).

[5] D. Gonnella, R. Eichhorn, F. Furuta, M. Ge, D. Hall, V. Ho, G. Hoffstaetter, M. Liepe, T. O'Connell, S. Posen, P. Quigley, J. Sears, V. Veshcherevich, A. Grassellino, A. Romanenko, and D. A. Sergatskov, Nitrogen-doped 9-cell cavity performance in a test cryomodule for LCLS-II, J. Appl. Phys. **117**, 023908 (2015).

[6] M. Martinello, , M. Checchin, , A. Grassellino, , A. C. Crawford, , O. Melnychuk, , A. Romanenko, and D. A. Sergatskov, Magnetic flux studies in horizontally cooled elliptical superconducting cavities, J. Appl. Phys. **118**, 044505 (2015).

[7] J.-M. Vogt, O. Kugeler, and J. Knobloch, High-Q operation of superconducting rf cavities: Potential impact of thermocurrents on the rf surface resistance, Phys. Rev.

ST Accel. Beams **18**, 042001 (2015).

[8] T. Kubo, Flux trapping in superconducting accelerating cavities during cooling down with a spatial temperature gradient, Prog. Theor. Exp. Phys. **2016**, 053G01 (2016).

[9] P. Kneisel, G. Ciovati, P. Dhakal, K. Saito, W. Singer, X. Singer, and G. R. Myneni, Review of ingot niobium as a material for superconducting radiofrequency accelerating cavities, Nucl. Instrum. Meth. A **774**, 133 (2015).

[10] S. Huang, T. Kubo, and R. L. Geng, Dependence of trapped-flux-induced surface resistance of a large-grain Nb superconducting radio-frequency cavity on spatial temperature gradient during cooldown through T_c, Phys. Rev. Accel. Beams **19**, 082001 (2016).

[11] A. S. Dhavale, P. Dhakal, A. A. Polyanskii, and G. Ciovati, Flux pinning characteristics in cylindrical niobium samples used for superconducting radio frequency cavity fabrication, Supercond. Sci. Technol. **25**, 065014 (2012).

[12] S. Posen, M. Checchin, A. C. Crawford, A. Grassellino, M. Martinello, O. S. Melnychuk, A. Romanenko, D. A. Sergatskov, and Y. Trenikhina, Efficient expulsion of magnetic flux in superconducting radiofrequency cavities for high Q_0 applications, J. Appl. Phys. **119**, 213903 (2016).

[13] A. M. Campbell and J.E. Evetts, Flux vortices and transport currents in type-II superconductors, Adv. Phys. **21**, 199 (1972).

[14] G. Ciovati, Effect of low-temperature baking on the radio-frequency properties of niobium superconducting cavities for particle accelerators, J. Appl. Phys. **96**, 1591 (2004).

[15] D. Gonnella, J. Kaufman, and M. Liepe, Impact of nitrogen doping of niobium superconducting cavities on the sensitivity of surface resistance to trapped magnetic flux, J. Appl. Phys. **119**, 073904 (2016).

[16] M. Martinello, A. Grassellino, M. Checchin, A. Romanenko, O. Melnychuk, D. A. Sergatskov, S. Posen, and J. F. Zasadzinski, Effect of interstitial impurities on the field dependent microwave surface resistance of niobium, Appl. Phys. Lett.**109**, 062601 (2016).

[17] M. Checchin, M. Martinello, A. Grassellino, S. Aderhold, S. K. Chandrasekaran, O. S. Melnychuk, S. Posen, A. Romanenko, and D. A. Sergatskov, Frequency dependence of trapped flux sensitivity in SRF cavities, Appl. Phys. Lett. **112**, 072601 (2018).

[18] B. Aune *et al.*, Superconducting TESLA cavities, Phys. Rev. ST Accel. Beams 3, 092001 (2000).

[19] G. Ciovati, P. Dhakal, and G. R. Myneni, Superconducting radio-frequency cavities made from medium and low-purity niobium ingots, Supercond. Sci. Technol. **29**, 064002 (2016).

[20] R. L. Geng, J. K. Hao, K. X. Liu, H. Y. Zhao, C. Adolphsen, and Z. Li, New results of development of high efficiency high gradient superconducting RF cavities, in*Proc. 6th International Particle Accelerator Conference (IPAC'15)*, Richmond, VA, USA, May 3-8, 2015, pp. 3518–3520, `doi:10.18429/JACoW-IPAC2015-WEPWI013`.

[21] H. Shimizu *et al.*, Fabrication and evaluation of superconducting single-cell cavities manufactured using various materials and methods, IEEE Trans. Appl. Supercond. **27**, 3500714 (2017).

[22] COMSOL Multiphysics modeling software, https://www.comsol.com/

[23] D. C. Mattis and J. Bardeen, Theory of the anomalous skin effect in normal and superconducting metals, Phys. Rev. **111**, 412 (1958).

[24] A. Gurevich, Theory of RF superconductivity for resonant cavities, Supercond. Sci. Technol. **30**, 034004 (2017).

[25] A. Gurevich and T. Kubo. Surface impedance and optimum surface resistance of a superconductor with an imperfect surface. Phys. Rev. B **96**, 184515 (2017).

[26] G. E. H. Reuter and E. H. Sondheimer, Theory of anomalous skin effect in metals, Proc. Roy. Soc. A**195**, 336 (1948).

[27] W. Jauch and M. Reehuis, Electron density distribution in vanadium and niobium from γ-ray diffraction, Phys. Rev. B**83**, 115102 (2011).

[28] A Miyazaki and W. Venturini Delsolaro, Determination of the Bardeen-Cooper-Schrieffer material parameters of the HIE-ISOLDE superconducting resonator, Supercond. Sci. Technol. **32**, 025002 (2019).

[29] A. Romanenko, A. Grassellino, F. Barkov, A. Suter, Z. Salman, and T. Prokscha, Strong Meissner screening change in superconducting radio frequency cavities due to mild baking, Appl. Phys. Lett. **104**, 072601 (2014).

[30] J. P. Carbotte, Properties of boson-exchange superconductors, Rev. Mod. Phys. **62**, 1027 (1990).

[31] A. Romanenko and D. I. Schuster, Understanding quality factor degradation in superconducting niobium cavities at low microwave field amplitudes, Phys. Rev. Lett. **119**, 264801 (2017).

[32] A. Gurevich and G. Ciovati, Effect of vortex hotspots on the radio-frequency surface resistance of superconductors, Phys. Rev. B **87**, 054502 (2013).

[33] A. Gurevich and G. Ciovati, Dynamics of vortex penetration, jumpwise instabilities, and nonlinear surface resistance of type-II superconductors in strong rf fields, Phys. Rev. B **77**, 104501 (2008).

[34] G. Blatter, M. V. Feigel'man, V. B. Geshkenbein, A. I. Larkin, and V. M. Vinokur, Vortices in high temperature superconductors, Rev. Mod. Phys. **66**, 1125 (1994).

[35] E.H. Brandt, The flux-line lattice in superconductors, Rep. Prog. Phys. **58**, 1465 (1995).

[36] M. Checchin, M. Martinello, A. Grassellino, A. Romanenko and J. F. Zasadzinski, Electron mean free path dependence of the vortex surface impedance, Supercond. Sci. Technol. **30**, 034003 (2017).

[37] S. Calatroni and R. Vaglio, Simple model for the rf field amplitude dependence of the trapped flux sensitivity in superconducting rf cavities, Phys. Rev. Accel. Beams **22**, 022001 (2019).

[38] J. I. Gittleman and B. Rosenblum, Radio-frequency resistance in the mixed state for subcritical currents, Phys. Rev. Lett. **16**, 734 (1966).

[39] A. Gurevich, Pinning size effects in critical currents of superconducting films. Supercond. Sci. Technol. **20**, S128 (2007).

[40] R. Willa, V. B. Geshkenbein, and G. Blatter, Probing the pinning landscape in type-II superconductors via Campbell penetration depth, Phys. Rev. B **93**, 064515 (2016).

[41] D. B. Liarte, D. Hall, P. N. Koufalis, A. Miyazaki, A. Senanian, M. Liepe, and J. P. Sethna, Vortex Dynamics and Losses Due to Pinning: Dissipation from Trapped Magnetic Flux in Resonant Superconducting Radio-Frequency Cavities, Phys. Rev. Applied **10**, 054057 (2018).

[42] Matthias Liepe, Cornell University, private communication.

[43] A. Grassellino, N doping: progress in development and understanding, in*Proc. of the 17th International Conference on RF Superconductivity (SRF2015)*, Vancouver, BC, Canada, September 13-18, 2015, pp. 48–54, doi:10.18429/JACoW-SRF2015-MOBA06.

[44] J. Tuggle, U. Pudasaini, F. A. Stevie, M. J. Kelley, A. D. Palczewski and C. E. Reece, Secondary ion mass spectrometry for superconducting radiofrequency cavity materials, J. Vac. Sci. Technol. B **36**, 052907 (2018).

[45] A. Romanenko and H. Padamsee, The role of near-surface dislocations in the high magnetic field performance of superconducting niobium cavities, Supercond. Sci. Technol. **23**, 045008 (2010).

[46] B. Visentin, M. F. Barthe, V. Moineau, and P. Desgardin, Involvement of hydrogen-vacancy complexes in the baking effect of niobium cavities, Phys. Rev. ST Accel. Beams **13**, 052002 (2010).

[47] N.B. Kopnin, *Theory of nonequilibrium superconductivity.* (Oxford Univ. Press, 2001).

[48] E. V. Thuneberg, J. Kurkijärvi, and D. Rainer, Elementary-flux-pinnng potential in type-II superconductors, Phys. Rev. B **29**, 3913 (1984).

[49] C. J. van der Beek and P. H. Kes, Dislocation-mediated flux creep in $Bi_2Sr_2CaCu_2O_{8+\delta}$, Phys. Rev. B **43**, 13032 (1991).

[50] The cavity was labeled LG-4 in [21]